The Planetary Science Journal, 2:13 (15pp), 2021 February https://doi.org/10.3847/PSJ/abd258

Chromium Isotopic Evidence for Mixing of NC and CC Reservoirs in Polymict Ureilites: Implications for Dynamical Models of the Early Solar System

Cyrena A. Goodrich[1], Matthew E. Sanborn[2], Qing-Zhu Yin[2], Issaku Kohl[3], David Frank[4], R. Terik Daly[5], Kevin J. Walsh[6], Michael E. Zolensky[7], Edward R. D. Young[3], Peter Jenniskens[8], and Muawia H. Shaddad[9]
[1] Lunar and Planetary Institute, Universities Space Research Association, 3600 Bay Area Boulevard, Houston, TX 77058, USA; goodrich@lpi.usra.edu
[2] Department of Earth and Planetary Sciences, University of California at Davis, Davis, CA 95616, USA
[3] Department of Earth and Planetary Sciences, University of California at Los Angeles, 595 Charles Young Drive East, Los Angeles, CA 90095, USA
[4] Hawai'i Institute of Geophysics and Planetology, Department of Earth Sciences, University of Hawai'i at Mānoa, Honolulu, HI 96822, USA
[5] The Johns Hopkins University Applied Physics Laboratory, 11100 Johns Hopkins Road, Laurel, MD 20723, USA
[6] Southwest Research Institute, 1050 Walnut Street, Suite 300, Boulder, CO 80302, USA
[7] Astromaterials Research and Exploration Science, NASA Johnson Space Center, Houston, TX 77058, USA
[8] SETI Institute, 189 Bernardo Avenue, Mountain View, CA 94043, USA
[9] Physics Department, University of Khartoum, Khartoum 11115, Sudan
Received 2020 September 1; revised 2020 November 18; accepted 2020 December 7; published 2021 January 28

Abstract

Nucleosynthetic isotope anomalies show that the first few million years of solar system history were characterized by two distinct cosmochemical reservoirs, CC (carbonaceous chondrites and related differentiated meteorites) and NC (the terrestrial planets and all other groups of chondrites and differentiated meteorites), widely interpreted to correspond to the outer and inner solar system, respectively. At some point, however, bulk CC and NC materials became mixed, and several dynamical models offer explanations for how and when this occurred. We use xenoliths of CC materials in polymict ureilite (NC) breccias to test the applicability of such models. Polymict ureilites represent regolith on ureilitic asteroids but contain carbonaceous chondrite-like xenoliths. We present the first ^{54}Cr isotope data for such clasts, which, combined with oxygen and hydrogen isotopes, show that they are unique CC materials that became mixed with NC materials in these breccias. It has been suggested that such xenoliths were implanted into ureilites by outer solar system bodies migrating into the inner solar system during the gaseous disk phase ~3–5 Myr after CAI, as in the "Grand Tack" model. However, combined textural, petrologic, and spectroscopic observations suggest that they were added to ureilitic regolith at ~50–60 Myr after CAI, along with ordinary, enstatite, and Rumuruti-type chondrites, as a result of the breakup of multiple parent bodies in the asteroid belt at this time. This is consistent with models for an early instability of the giant planets. The C-type asteroids from which the xenoliths were derived were already present in inner solar system orbits.

Unified Astronomy Thesaurus concepts: Dynamical evolution (421); Meteorites (1038); Achondrites (15); Impact phenomena (779); Isotopic abundances (867)

1. Introduction and Background

Nucleosynthetic isotope anomalies in a number of elements (including Cr, Ti, Mo, W, Ru, and Ni) show that solar system materials are starkly divided into two suites, referred to as CC and NC (Trinquier et al. 2007, 2009; Yin et al. 2009; Burkhardt et al. 2011; Warren 2011; Budde et al. 2016; Kruijer et al. 2017; Poole et al. 2017; Nanne et al. 2019; Sanborn et al. 2019; Worsham et al. 2019; Williams et al. 2020). The CC suite includes all carbonaceous chondrites (CC per se), some iron meteorite groups, and some ungrouped achondrites. The NC suite includes terrestrial, lunar, and Martian samples, as well as ordinary, enstatite, and Rumuruti-type chondrites (OC, EC, and RC), some iron meteorite groups, all major groups of achondrites, and some ungrouped meteorites (e.g., Figure 1). This large-scale division suggests that the earliest solar system was characterized by two distinct cosmochemical reservoirs, which remained isolated from one another for a least a few million years (Warren 2011; Budde et al. 2016; Kruijer et al. 2017; Worsham et al. 2019). The prevailing interpretation of these two reservoirs is that they correspond to the inner (NC) versus the outer (CC) solar system, with the barrier between them being created by the growth of Jupiter (Kruijer et al. 2017) or a pressure maximum in the gaseous disk (Brasser & Mojzsis 2020), although Huss (2019) argued that there is no evidence actually requiring a correspondence to inner and outer solar system locations for the two reservoirs.

Regardless of how the NC–CC dichotomy was established in the earliest solar system, it is clear that bulk NC and CC materials became mixed with one another at a later time or times. Definitive evidence for such mixing on a large scale comes from the observations that CC meteorites have made it to Earth, and that the asteroid belt contains not only inferred NC (e.g., S, E, and V) asteroid types but also inferred CC (i.e., C and B) types. Under the assumption that the NC versus CC dichotomy corresponds to inner versus outer solar system formation locations, these observations imply long-distance migration of CC bodies from beyond the orbit of Jupiter into the inner solar system. Several types of dynamical models offer explanations for how and when this could have occurred. One type of model focuses on the dynamics of early solar system bodies during the gaseous disk phase, i.e., ⩽5 Myr after CAI. For example, the "Grand Tack" hypothesis (Walsh et al. 2011, 2012) posits that during the gaseous disk period, Jupiter migrated into the inner solar system and then back out, resulting in major migrations of both inner solar system ("S-type") and outer solar system ("C-type" from between the orbits of Jupiter and Saturn) bodies and leaving a

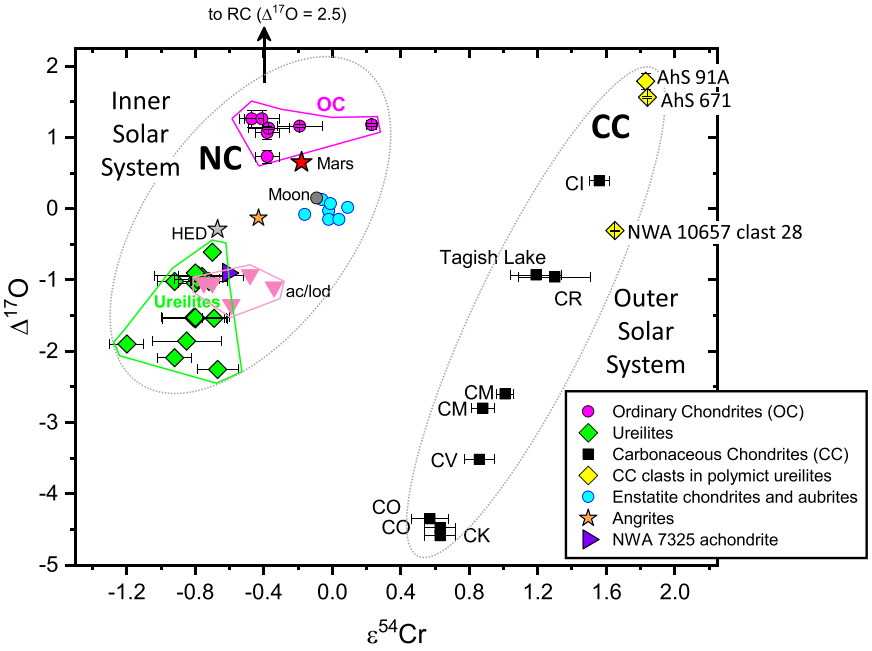

Figure 1. Plot of ε^{54}Cr vs. Δ^{17}O, on which solar system materials show a stark dichotomy between the CC suite, consisting mainly of carbonaceous chondrites (plus some differentiated meteorites not shown here), and the NC suite, consisting of Earth, the Moon, Mars, ordinary chondrites, enstatite chondrites, Rumuruti-type chondrites, and most major groups of achondrites, including angrites, acapulcoites and lodranites (ac/lod), and the HED group. The currently prevailing interpretation of these two suites is that they correspond to materials that formed in the outer solar system vs. the inner solar system, respectively (Warren 2011; Kruijer et al. 2017). Polymict ureilites are NC breccias that contain xenoliths of carbonaceous chondrite-like materials. Chromium and oxygen isotope data obtained here for three such xenoliths (yellow diamonds) show that they are derived from the CC isotopic reservoir, providing ground-truth evidence for mixing of bulk CC materials into NC asteroidal regoliths. Sources of data (alphabetical order): Clayton & Mayeda (1996, 1999), Clayton et al. (1984, 1991), Dauphas & Schauble (2016), Goodrich et al. (2017a), Jenniskens et al. (2012, 2014), Li et al. (2018), Popova et al. (2013), Qin et al. (2010), Rubin et al. (2002), Shukolyukov & Lugmair (2006), Trinquier et al. (2007), Ueda et al. (2006), Yamakawa et al. (2010).

configuration of mixed asteroid taxonomic types similar to the present distribution in the asteroid belt. An alternative set of models suggests that the scattering of bodies from beyond Jupiter into the asteroid belt during the gaseous disk period is simply a result of rapid giant planet formation (Kretke et al. 2017; Raymond & Izidoro 2017). In fact, Raymond & Izidoro (2017) showed that migration of "C-type" bodies into the inner solar system is a natural consequence of the growth of giant planets in the gaseous disk phase and is not specifically tied to the growth mechanism.

A second type of model focuses on solar system dynamics after dispersion of the gaseous disk. For example, the "Nice Model" (Gomes et al. 2005; Morbidelli et al. 2005; Tsiganis et al. 2005) posits a period of "global" instability 400–700 Myr after the dispersion of the gas disk (the time being poorly constrained), during which some trans-Neptunian bodies (inferred D- and P-type asteroids) would have been transferred into the outer asteroid belt (Levison et al. 2009; Vokrouhlický et al. 2016). Recently, it has been argued that the "Nice Model"–type instability occurred much earlier (referred to as the "Early Instability" throughout), within ~100 Myr of the dispersion of the gas disk during the period of terrestrial planet formation (Clement et al. 2018, 2019; de Sousa et al. 2020).

Thus, dynamical models offer several possible explanations for the current mix of asteroid types in the asteroid belt. However, in the absence of knowledge of the isotopic compositions of asteroids in the asteroid belt, or the provenance of the CC meteorites that have arrived at Earth, it is not possible to definitely test such models, e.g., to evaluate whether they support the paradigm of NC versus CC = inner versus outer solar system formation, or to evaluate competing models, such as the Nice Model versus Early Instability.

Here we utilize a unique source of ground-truth information that can help us to do this: xenoliths of CC-like materials that occur in NC meteorite breccias. Several types of NC meteorite breccias, including OC, RC, howardite–eucrite–diogenite (HED) breccias, and polymict ureilites contain xenoliths (i.e., foreign clasts) of CC-like materials (Fredriksson et al. 1969; Fodor & Keil 1976; Fodor et al. 1976; Keil & Fodor 1980; Jaques & Fitzgerald 1982; Nozette & Wilkening 1982; Prinz et al. 1987; Brearley & Prinz 1992; Zolensky et al. 1996; Ikeda et al. 2000, 2003; Gounelle et al. 2003, 2005; Goodrich et al. 2004, 2019a, 2019b, 2020; Rubin & Bottke 2009; Funk et al. 2011; Greshake 2014; Bischoff et al. 2018b; Patzek et al. 2018; Hamilton et al. 2020a, 2020b). In general, xenoliths in meteoritic breccias are interpreted as surviving fragments of impactors that collided with their host meteorite parent bodies (e.g., Keil & Fodor 1980; Bischoff et al. 2006; Rubin & Bottke 2009; Goodrich et al. 2015a). As such, they can provide information about impact conditions and timing, as well as the types of impacting materials, and thus can be used to test or inform models of early solar system dynamics. Several authors have suggested that implantation of CC-like xenoliths into NC breccias was associated with one or another of the dynamical models described above. Yin et al. (2018) argued that the Grand Tack migration was responsible for implanting CC-like materials into polymict ureilites. Zolensky et al. (2008) suggested that the Nice Model instability may have been responsible for implanting micrometeorites and some CC-like xenoliths into HED and OC breccias.

However, although CC-like xenoliths in NC breccias have been described as CM-, CI-, or CR-like based on mineralogy (Zolensky et al. 1996; Rubin et al. 2002; Gounelle et al. 2003; Rubin & Bottke 2009; Patzek et al. 2018), their identity as members of the CC isotopic reservoir (Figure 1) has not been definitely established. Furthermore, a lack of definitive information on the timing of implantation of xenoliths has hindered linking them to specific dynamical models.

Here we present the first Cr isotope data for CC-type xenoliths in polymict ureilites (previously reported in abstracts; Sanborn et al. 2017; Yin et al. 2018; Goodrich et al. 2019b). Combined with oxygen isotope data, Cr isotope compositions show definitively that these xenoliths are samples of CC reservoir materials that became intimately mixed with a large variety of NC materials in ureilitic regolith. We also present hydrogen isotope and petrologic data, which, in combination with the chromium and oxygen data, show that these xenoliths represent unique solar system materials that are not present as whole meteorites in our collections.

Using the petrology and isotopic compositions of these xenoliths, as well as their textural relationships to other components of their host breccias, we examine (1) the timing of their implantation, (2) the conditions of their implantation (e.g., impact velocities), and (3) whether they are more likely related to C- or to D- and P-type asteroids. We then evaluate whether these xenoliths were likely to have been implanted into ureilitic regolith directly from outer solar system bodies migrating into the inner solar system or indirectly from CC bodies already present in orbits in the inner solar system, and what this tells us about proposed dynamical models. Finally, we consider whether these results support the prevailing view that the NC versus CC dichotomy corresponds to inner versus outer solar system formation locations.

1.1. Brief Background on Polymict Ureilites

Ureilites are a major group of ultramafic achondrites (Mittlefehldt et al. 1998) that represent a partially differentiated NC parent asteroid (Figure 1) and include polymict breccias that are interpreted to have formed in ureilitic regolith (Goodrich et al. 2004, 2015a; Downes et al. 2008; Herrin et al. 2010). Polymict ureilites are fragmental breccias dominated by clasts of mixed ureilitic materials but also have a notably high abundance of xenoliths (up to ~10 vol. %), including multiple types of chondrites and achondrites (Jaques & Fitzgerald 1982; Prinz et al. 1986, 1987; Ikeda et al. 2000, 2003; Goodrich et al. 2004, 2015a, 2015b, 2016, 2017a, 2017b, 2019a, 2019b, 2020; Bischoff et al. 2006; Downes et al. 2008; Ross et al. 2010; Horstmann & Bischoff 2014; Goodrich & Gross 2015; Patzek et al. 2018; Boleaga & Goodrich 2019). The CC-like xenoliths are some of the largest and most abundant of these.

The Almahata Sitta (AhS) anomalous polymict ureilite fell in 2008 when asteroid 2008 TC_3 entered Earth's atmosphere over northern Sudan (Jenniskens et al. 2009; Shaddad et al. 2010). The asteroid disintegrated in the atmosphere, with most of its mass being lost and only its strongest clasts surviving to become the recovered AhS stones (Jenniskens et al. 2009; Goodrich et al. 2015a). These stones are notably diverse, consisting of 70%–80% ureilites and 20%–30% various types of chondrites (Horstmann & Bischoff 2014; Bischoff et al. 2015, 2016, 2018a, 2019; Goodrich et al. 2015a, 2018, 2019a, 2019b). The diversity of materials in AhS resembles that found in typical polymict ureilites, consistent with 2008 TC_3 being a sample of loosely consolidated regolith from the same body as typical polymict ureilites (Goodrich et al. 2015a, 2019a). Stones AhS 91A and 671 (two of the samples included in this study) were the first stones from AhS showing contacts between ureilitic and chondritic lithologies (Goodrich et al. 2019a), providing critical observations that support this interpretation.

2. Samples and Methods

AhS 91A and AhS 671 are two stones of similar lithology from the University of Khartoum (UoK) collection of the Almahata Sitta meteorite (Shaddad et al. 2010) and were described in detail in Goodrich et al. (2019a). Small fragments of AhS 91A (AhS 91A_07) and AhS 671 (AhS 671_05) were used for Cr isotope analyses. Optical microscope observations of these fragments showed only the dominant C1 lithology of these stones (Goodrich et al. 2019a). Hydrogen isotope analyses were conducted on polished sections AhS 91A_01, AhS 671_02, and AhS 671_03.

Northwest Africa (NWA) 10657 is a typical polymict ureilite consisting mostly of clasts of various ureilitic materials but also containing foreign clasts of diverse types (Bouvier et al. 2017; Goodrich et al. 2017a). We have studied three polished thin sections and a cut slab of NWA 10657 and here describe two CC-like clasts from section _001. In addition, NWA 10657 clast 28 was observed on the polished slab and then extracted (see the Appendix). The extracted clast was divided into aliquots for chromium and oxygen isotope analyses, and the remaining fragment was prepared as a polished mount (~0.4 mm^2) for detailed scanning electron microscopy (SEM) and electron microprobe analysis (EMPA) studies. Hydrogen isotope analyses were obtained on two clasts in the polished thin section NWA 10657_001. All analytical techniques are described in the Appendix.

3. Results

3.1. Petrology

The petrology of AhS 91A and AhS 671, described in detail in Goodrich et al. (2019a), is summarized here. These stones are dominated volumetrically by a C1 lithology that consists of fine-grained phyllosilicates (serpentine and saponite) and amorphous material, magnetite, carbonates (breunnerite and dolomite), fayalitic olivine (Fo 28–42), an unidentified Ca-rich silicate phase (not previously reported in any CC), Fe,Ni sulfides (both as coarse grains and abundant finely dispersed grains in matrix), and minor Ca-phosphate and ilmenite. Relative proportions of these phases and compositions of phyllosilicates (Figure 2(a)) vary, with some areas appearing to be distinct clasts. In particular, some areas consist almost entirely of phyllosilicates with none of the other phases. The sections of AhS 671 that we studied contain a higher proportion of fayalitic olivine than most of AhS 91A, but they also have areas with a relatively lower abundance of this phase. The general features of these samples, including overall mineralogy, and carbonate and magnetite compositions, are more like those of CI1 than any other known CC types. However, the presence of a significant amount of fayalitic olivine occurring as porous, tabular crystals and distinctive fayalite–magnetite clusters (Figure 3(b)), and the common occurrence of the Ca-rich silicate phase as patchy or fibrous aggregates or tabular crystals (Figure 3(a)) make these lithologies unique. The Ca-rich silicate phase (Table 1) has EMPA totals of ~94%–97%, indicating that it contains less OH

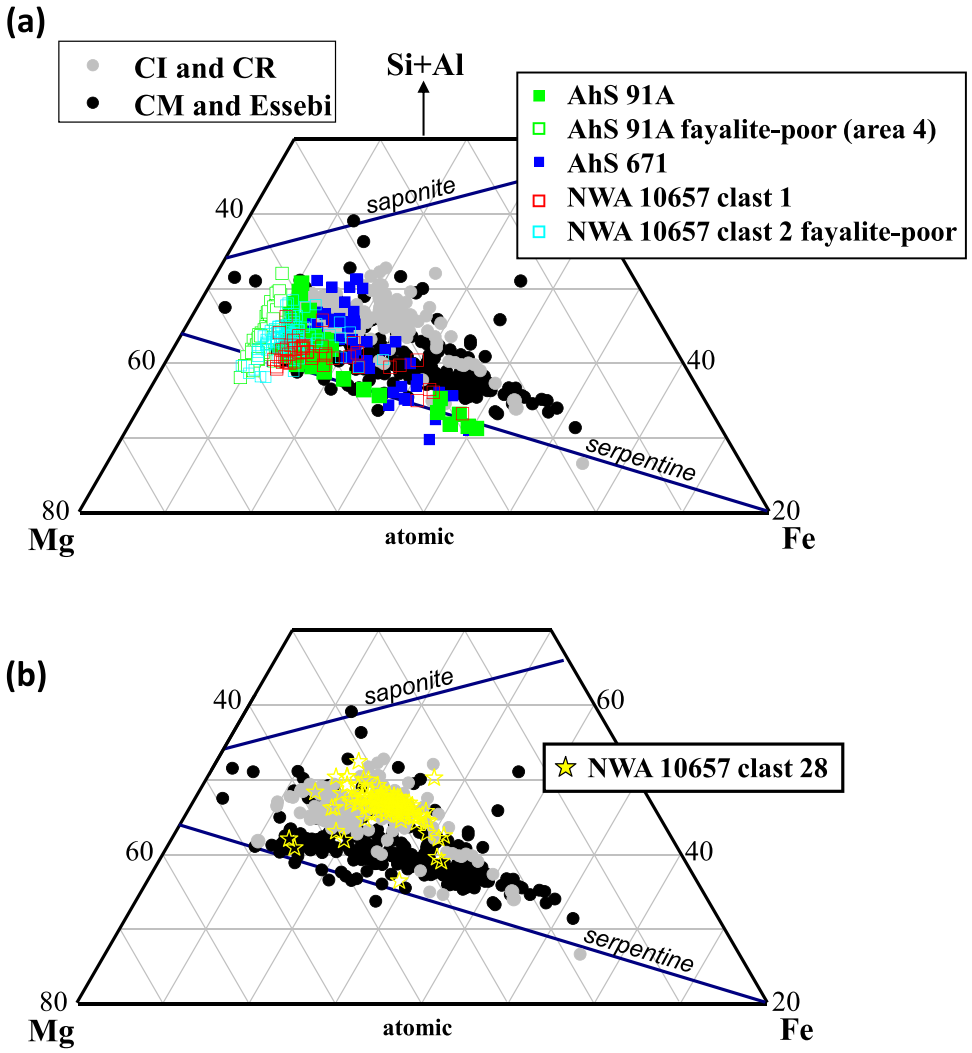

Figure 2. Shown are (Si+Al)–Mg–Fe atomic percent ternary diagrams plotting compositions of phyllosilicates in AhS 91A, AhS 671, and three CC-like xenoliths in polymict ureilite NWA 10657 compared with those in CI, CR, and CM carbonaceous chondrites. Lines represent observed stoichiometric compositions of serpentine and saponite solid solution series (Deer et al. 1962; Fleet 2003). Data for xenoliths were obtained by line scans of broad-beam analyses of matrix areas and then filtered to remove analyses with high FeO (presumably including magnetite and/or fayalite and/or sulfides) and CaO (including Ca-rich phases), as well as those with extremely low totals. Data for AhS 91A, AhS 671, and CC are from Goodrich et al. (2019a).

than serpentine or smectite, but it contains far too much CaO (~12–18 wt.%) to be (only) a dehydrated version of either of these phyllosilicates. Focused ion beam/transmission electron microscopy (FIB/TEM) analyses of this "phase" showed Ca-rich, poorly crystalline material containing flakes of a layered phase with a basal spacing of 0.95–0.96 nm, which would be correct for completely dehydrated smectites. Thus, Goodrich et al. (2019a) hypothesized that the Ca-rich silicate phase is an assemblage of dehydrated smectite plus at least one other phase, possibly including heated (calcined) carbonates. It contains ~0.5–1 wt.% P_2O_5, which may be due to tiny inclusions of Ca-phosphate. Another distinctive feature of AhS 91A is that bulk matrix phyllosilicate compositions have a lower apparent smectite component than CI chondrites (Figure 2(a)).

The C1 lithology in AhS 91A and AhS 671 encloses rounded to angular clasts (<10 μm to 3 mm) of olivine, pyroxenes, plagioclase, graphite, and metal-sulfide, as well as chondrules (~130–600 μm) and chondrule fragments. These components are exogenous with respect to the C1 lithology and have been identified from petrology and oxygen isotope compositions as a mixture of ureilitic mineral fragments, OC chondrules and mineral fragments, and both OC and EC metal (Goodrich et al. 2019a). Some aspects of these materials not discussed in Goodrich et al. (2019a) will be discussed here.

NWA 10657 clast 1 is the largest non-ureilitic clast (~3 mm in longest dimension) in section NWA 10657_001 (Figure 4(a)). In general, it is similar to AhS 91A and even more so to AhS 671, with distinctive similarities including abundant fayalitic olivine in fibrous and/or porous morphologies (Figure 4(f)) and as rims around magnetite grains (Figure 4(b)), as well as grains and fibrous/tabular crystals of a Ca-rich silicate phase very similar in morphology and composition to that in AhS 91A (Figures 4(c) and (e); Table 1). As in AhS 91A and AhS 671, the abundances of the phases vary from place to place, with a number of areas or patches showing no fayalitic olivine (e.g., Figure 4(f), right side). One notable feature (not seen in AhS 91A or 671) is a cluster of grains of ilmenite, Ca-phosphate, and the Ca-rich silicate (Figures 4(d) and (e)). Matrix phyllosilicate compositions (i.e., broad-beam analyses of the matrix) are also similar to those in AhS 91A and AhS 671 (Figure 2(a)). No carbonates or coarse-grained sulfides were observed.

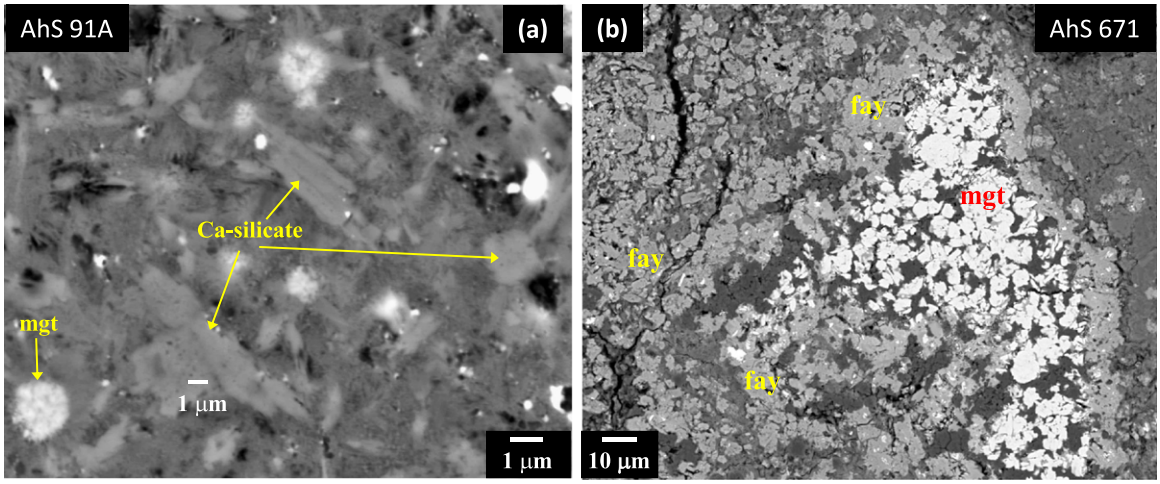

Figure 3. BEIs of some distinctive mineralogical features of AhS 91A and AhS 671. (a) A currently unidentified Ca-rich silicate phase commonly occurs as fibrous laths and clumps. (b) Fayalite-rich olivine (Fo ~20–30) occurs as fibrous laths and clumps, and also commonly as rims around grains or aggregates of grains of magnetite. Abbreviations: mgt = magnetite; fay = fayalitic olivine.

Table 1
Compositions of Phases (wt.% Oxides) in Studied Clasts from EMPA

	AhS 91A	NWA 10657 Clast 1				NWA 10657 Clast 28	
	Ca- silicate	Ca-silicate (7)	phos	ilm	mag[a]	oliv	oliv
SiO_2	47.3	48.5	0.6	0.1	0.04	41.6	38.7
TiO_2	0.02	0.11	0.10	52.4	bdl	bdl	bdl
Al_2O_3	3.8	2.4	bdl	bdl	0.02	0.34	0.03
Cr_2O_3	0.47	0.40	0.02	0.18	0.07	0.27	0.35
FeO	9.2	7.3	2.0	43.4	30.8	0.84	23.8
Fe_2O_3					68.4		
MgO	18.3	17.3	2.2	0.20	0.05	57.8	39.1
MnO	0.23	0.33	0.06	4.0	0.06	0.36	0.24
CaO	13.7	17.8	52.1	0.11	0.04	0.12	0.19
NiO	0.19	na	na	0.04	0.02	0.15	0.20
Na_2O	2.93	1.53	0.11	bdl	bdl	bdl	bdl
K_2O	0.04	0.01	bdl	bdl	bdl	bdl	bdl
P_2O_5	0.79	1.30	40.7	bdl	bdl	bdl	bdl
SO_3	bdl	0.11	bdl	bdl	bdl	bdl	bdl
Total	97.0	97.0	97.9	100.4	99.5	101.5	102.6
Mg#						99.2	74.6

Notes. oliv = olivine; phos = phosphate; ilm = ilmenite; mag = magnetite, bdl = below detection limit; na = not analyzed, Mg# = molar MgO/(MgO + FeO).
[a] Recalculated assuming molar $Fe^{2+}/Fe^{3+} = 2/3$.

NWA 10657 clast 2 is ~700 μm in longest dimension and consists mostly of a phyllosilicate matrix with abundant clusters and tabular crystals of porous, fayalitic olivine, similar to some areas of AhS 91A and most of AhS 671, as well as clumps and sprays of the Ca-rich silicate (Figure 4(g)). Sparse breunnerite (of similar composition to that in AhS 91A and AhS 671) and Fe,Ni sulfide grains occur. Magnetite was not observed. A few areas that appear to be pure phyllosilicates (Figure 4(g), right side) showed compositions similar to the most magnesian phyllosilicates in AhS 91A and AhS 671 (Figure 2(a)).

NWA 10657 clast 28 consists predominantly of very fine-grained, spongy matrix material (little structure visible in SEM observations) containing common magnetite as clusters of euhedral and subhedral ⩽1 μm–sized crystals and framboids (Figure 5(a)), plus a few irregularly shaped ~10–20 μm–sized grains of olivine (Figure 5(b)) with compositions of both Fo ~98–99 (Table 1) and Fo ~75. Defocused beam analyses of the matrix suggest that it consists of a mix of serpentine and smectite with compositions typical for CI and CR chondrites and distinct from most phyllosilicates in AhS 91A and 671 (Figure 2(b)). The clast appears to have extremely low S content, as no sulfide grains were observed and all matrix analyses show very low S content (<0.1 wt.%).

3.2. Chromium and Oxygen Isotope Compositions

Chromium and oxygen isotope compositions for bulk samples of AhS 91A, AhS 671, and NWA 10657 clast 28 are given in Table 2 and shown in Figure 1. All three samples are clearly associated with the CC suite. Stones AhS 91A and AhS 671 have very similar compositions, with higher ε^{54}Cr and Δ^{17}O than any major CC group. In a recent abstract, Patzek et al. (2019) reported a higher ε^{54}Cr value of 2.84 ± 0.12 (at similar Δ^{17}O) for a CC-like clast from polymict ureilite Dar al Gani (DaG) 1064 but did not describe the petrology of this clast. The NWA 10657 clast 28 also shows a unique Δ^{17}O–ε^{54}Cr composition (Figure 1), but its ε^{54}Cr is similar to that of CI.

3.3. Hydrogen Isotope Compositions

The D/H ratios for the analyzed samples are given in Table 3 and shown in Figure 6. Because our measurements include little to no signal from the organic component (see the Appendix), which has much higher D/H than phyllosilicates in unmetamorphosed CCs (Alexander et al. 2007, 2010), our measurements represent lower limits for the bulk compositions. Therefore, our data cannot be directly compared with those of Patzek et al. (2017, 2020) for CC-like clasts in polymict ureilites, because their measurements reflect a mixed signal from organic matter and hydrated silicates.

The results we obtained for AhS 91A are remarkable (Figure 6). This sample shows higher D/H in its dominant matrix materials ($\delta D > 1380‰ \pm 66‰$) than any bulk CC previously studied, other than one anomalously high value for CO 3.4 Ornans (Kerridge 1985). Furthermore, in areas that appear to be nearly pure phyllosilicates, i.e., with relatively low abundances of fayalitic olivine, it shows even higher D/H

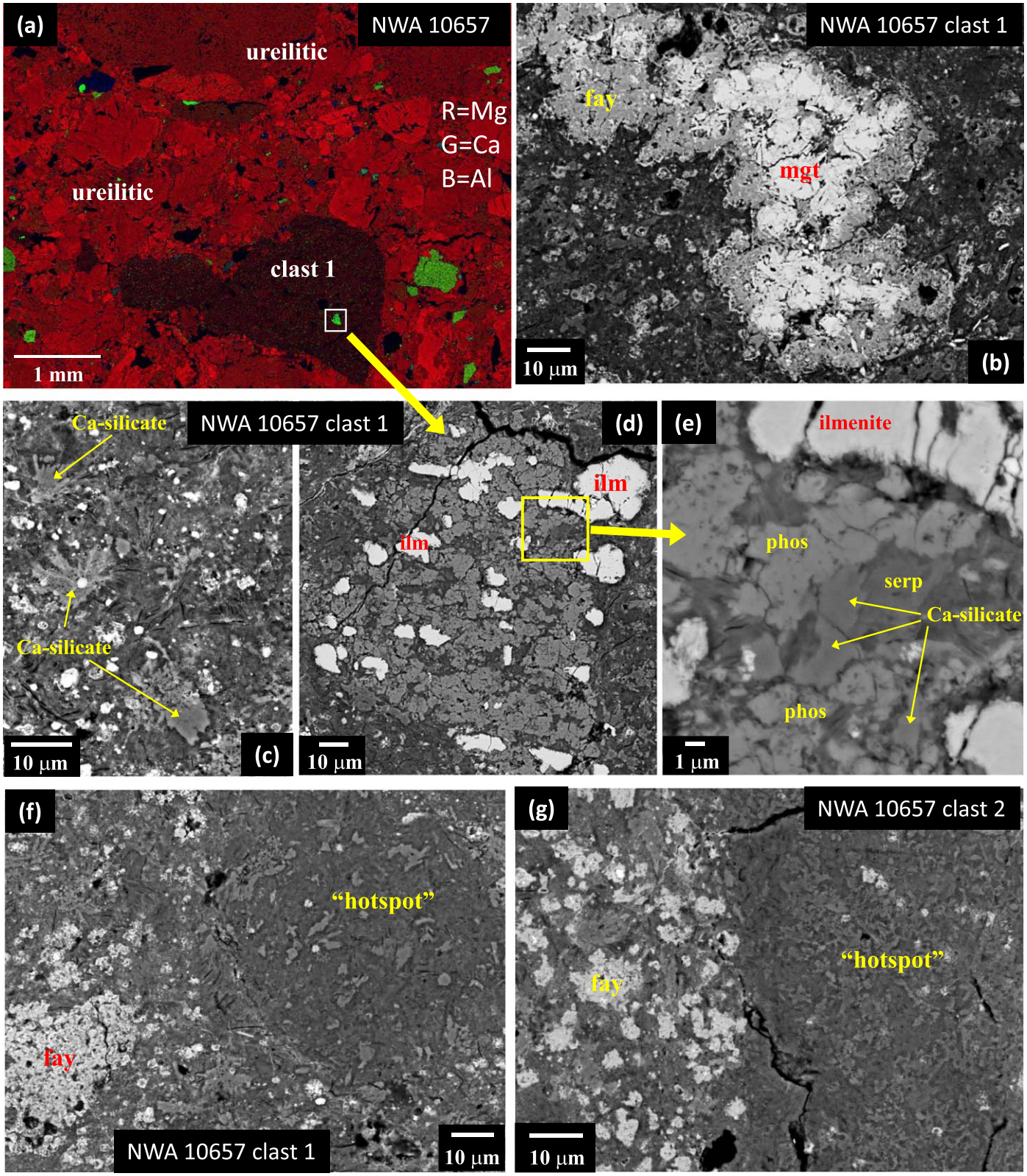

Figure 4. Combined elemental X-ray maps (a) and BEIs (others) of CC-like clasts 1 and 2 in polymict ureilite NWA 10657. (b) Aggregate of magnetite grains with rim of fayalitic olivine, similar to occurrences in AhS 91A and AhS 671 (see Figure 3(b) and also images in Goodrich et al. 2019a). (c) Sprays of the unidentified Ca-silicate phase, similar to occurrences in AhS 91A and AhS 671 (see Figure 3(a) and also images in Goodrich et al. 2019a). (d) and (e) Area outlined by box in panel (a) showing aggregate of grains of Ca-phosphate, ilmenite, and the Ca-rich silicate phase, along with some serpentine. (f) and (g) Areas with a low abundance of fayalitic olivine are labeled "hotspot" because they show a higher D/H ratio than the main matrix materials. Abbreviations: mgt = magnetite; fay = fayalitic olivine; phos = phosphate; ilm = ilmenite.

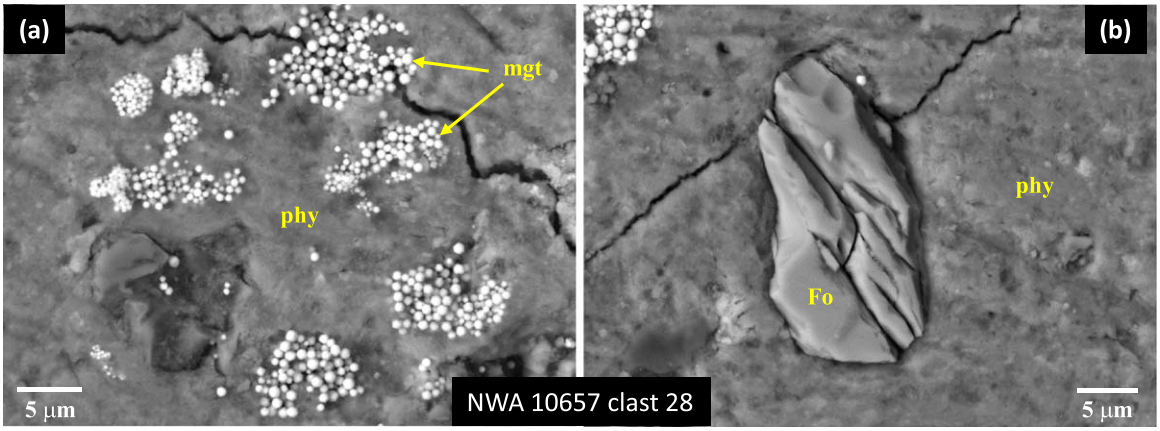

Figure 5. BEI of clast 28 extracted from polymict ureilite NWA 10657. (a) General appearance of clast, with very fine-grained phyllosilicate matrix (phy) and common clusters of grains and framboids of magnetite (mgt). (b) Grain of nearly pure forsteritic olivine (Fo).

Table 2
Chromium and Oxygen Isotope Compositions of Studied Clasts

Sample	ε^{53}Cr	ε^{54}Cr	δ^{17}O	δ^{18}O	Δ^{17}O
AhS 91A	0.09 ± 0.05	1.83 ± 0.08	8.931	13.531	1.792
AhS 671	0.04 ± 0.03	1.84 ± 0.07	7.308	10.872	1.567
NWA 10657 clast 28	0.21 ± 0.05	1.65 ± 0.12	10.356	20.195	−0.307

($\delta D = 1714‰ \pm 100‰$). Areas of nearly pure phyllosilicates (low abundance of fayalitic olivine) in clasts 1 and 2 show similarly high D/H ($\delta D = 1425‰ \pm 75‰$ and $1579‰ \pm 241‰$, respectively). The main matrix materials in AhS 671, clast 1, and clast 2 show lower D/H than AhS 91A, with average values similar to those of bulk CR and Tagish Lake (Figure 6). In AhS 671, areas that contain relatively less fayalitic olivine than most of the sample also show higher D/H than the main matrix materials (Figure 6). These results suggest a correlation of decreasing D/H ratio with increasing abundance of fayalitic olivine within each sample. This correlation also appears to hold among samples, since AhS 671, clast 1, and clast 2 all show higher overall abundances of fayalitic olivine than AhS 91A.

4. Discussion

4.1. Origin of CC-like Xenoliths in Polymict Ureilites

The chromium isotope data for AhS 91A, AhS 671, and NWA 10657 clast 28 (Figure 1) show that these xenoliths originate from the CC isotopic reservoir and thus constitute ground-truth evidence for mixing of bulk CC reservoir materials into NC regolith. Further, the mineralogy/petrology, along with combined chromium, oxygen, and hydrogen isotope data, for AhS 91A, AhS 671, and NWA 10657 clasts 1 and 2 show that these xenoliths represent a unique CC lithology (or several similar lithologies) not represented by whole meteorites in our collections.

Goodrich et al. (2019a) discussed the unique mineralogical features of AhS 91A and AhS 671 and argued that they could represent a common, heterogeneous lithology. The mineralogical features of NWA 10657 clasts 1 and 2 suggest that they derive from the same, or a very similar, lithology or lithologies. The common occurrence of fayalitic olivine, spatial variations in the strength of the hydration band as seen in micro-FTIR, and the partially dehydrated composition of the Ca-rich silicate phase, all indicate that this lithology, though more like CI than any other known CC group, has experienced heterogeneous thermal metamorphism (Zolotov et al. 2006; Goodrich et al. 2019a). Thermal metamorphism has previously been seen in two chondrites classified as CI, Y-86029 and Y-82162 (Tonui et al. 2014), though we note that King et al. (2019) recently suggested that even these metamorphosed stones are unrelated to CI chondrites. However, neither the Ca-rich silicate phase nor fayalitic olivine have been reported in Y-86029 or Y-82162 (Tonui et al. 2014). Furthermore, the oxygen isotope composition of AhS 91A (Table 2) is very different from the compositions of Y-86029 or Y-82162 ($\delta^{18}O = 21.89$, $\delta^{17}O = 11.59$, $\Delta^{17}O = 0.21$ and $\delta^{18}O = 21.56$, $\delta^{17}O = 11.59$, $\Delta^{17}O = 0.38$, respectively; Tonui et al. 2014). Thus, although these clasts in polymict ureilites may represent CC-like materials that have been thermally metamorphosed, they are distinct from Y-86029 and Y-82162. Our results contrast with Patzek et al. (2018), who reported that the CC-like clasts in polymict ureilites are mineralogically undistinguished from CI.

The high δD values obtained for AhS 91A overall, and the phyllosilicate-dominated areas of all four samples (Figure 6), suggest that this lithology formed from D-enriched fluids, and retained a higher proportion of these fluids than most known CCs. Again, because our measurements do not include the organic component, which is known to be significant in at least AhS 671 (Kebukawa et al. 2019), our values represent lower limits for bulk compositions of these samples. Thus (although it remains to be tested), our data may be consistent with those of Patzek et al. (2020), who found δD values of ~1000–3000 for CC-like clasts in polymict ureilites, suggesting that these materials do contain a significant organic component. Combined with the data of Patzek et al. (2017, 2020), D/H ratios clearly support a unique source (compared with known CC) for at least some of the CC-like clasts in polymict ureilites. The apparent anticorrelation between the abundance of fayalitic olivine and δD values observed in our samples suggests the possibility that thermal metamorphism in these materials resulted in the loss of D-enriched fluids from some regions, although the mechanism for such a process is not clear. Further investigations of mineralogy/petrology combined with targeted D/H measurements are needed to test this possibility. It is likely that the observed D/H ratios of these samples are a result of multiple processes.

Table 3
Hydrogen Isotope Compositions of Studied Clasts

Sample	Area	δD‰ Weighted Mean	Standard Error	Standard Deviation
AhS 91A	Fayalite-poor (area 4[a])	1714	100	71
AhS 91A	Main lithology	1380	66	110
AhS 671	Fayalite-poor area	657	190	165
AhS 671	Main lithology	498	41	77
NWA 10657 clast 1	Fayalite-poor "hot spot"	1425	75	65
NWA 10657 clast 1	Main lithology	831	87	144
NWA 10657 clast 2	Fayalite-poor "hot spot"	1579	241	241
NWA 10657 clast 2	Main lithology	519	102	144

Note.
[a] Section AhS 91A_1 (see Goodrich et al. 2019a, Figure 5(a)), area of nearly pure phyllosilicates.

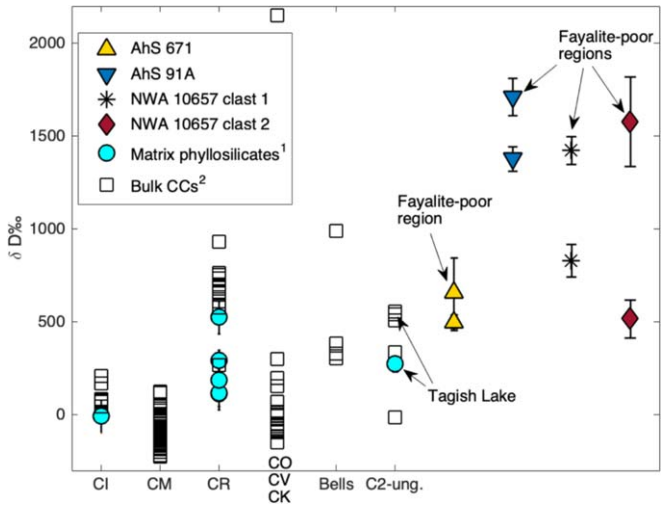

Figure 6. Hydrogen isotope compositions in CC xenoliths from polymict ureilites studied here, compared with matrix phyllosilicates in CCs and bulk CCs. The C2-ungrouped chondrites, in order of increasing δD, are Adelaide, Essebi, and Tagish Lake. The one anomalously high bulk δD value is from CO 3.4 Ornans (Kerridge 1985). [1]SIMS measurements of matrix phyllosilicates shown for Orgueil (CI) and Renazzo (CR2) from Piani et al. (2015), four CR chondrites from Bonal et al. (2013), and Tagish Lake from Engrand et al. (2003). The four CR values from Bonal et al. (2013) were calculated from the weighted mean of the reported spot measurements. [2]Bulk CC measurements were taken from Robert & Epstein (1982), Kerridge (1985), and Alexander et al. (2012, 2018).

This unique lithology (or group of similar lithologies) may be a common component in polymict ureilites, as more than half of the CC-like clasts examined in three polymict ureilites by Goodrich et al. (2019b) appear to belong to this group based on mineralogy, and a clast from the Nilpena polymict ureilite showed nearly identical oxygen isotope composition to AhS 91A (Brearley & Prinz 1992). Since some of the CC-like clasts studied by Patzek et al. (2017, 2019, 2020) in polymict ureilites show similar Cr isotopes and/or have high bulk D/H ratios, these clasts merit detailed mineralogical investigation to determine whether they are similar to the AhS 91A–like lithology.

It is important to note, however, that the AhS 91A/671–like lithology is not the only CC xenolith type in polymict ureilites. Both Patzek et al. (2018) and Goodrich et al. (2019b) noted a variety of types based on mineralogy. At least one of these is another unique CC lithology very different from AhS 91A (Hamilton et al. 2020a, 2020b; Goodrich et al. 2020). The petrology and combined chromium and oxygen isotope data for NWA 10657 clast 28 indicate that this clast represents yet another distinct CC lithology, although this one has greater similarities to known CI. It may be derived from a distinct source that was at a similar location to the CI source in the early solar system. In fact, none of the CC-like clasts described so far in polymict ureilites have been found to be identical to known CC types. This is in contrast to CC-like clasts in HED breccias, which are dominantly like CM2 chondrites (Zolensky et al. 1996; Gounelle et al. 2003; Patzek et al. 2018), suggesting that polymict ureilites may be sampling a different source (location and/or time) of CC material than other NC breccias.

The verification that CC-like xenoliths in polymict ureilites originate from the CC isotopic reservoir and, furthermore, represent unique materials not present among known meteorites, allows us to use these xenoliths as ground truth for evaluating dynamical models of the early solar system and addressing the origin of the NC versus CC dichotomy. To do this, we first evaluate the timing and conditions of implantation of the xenoliths into their host breccias.

4.2. Implantation of CC-like Xenoliths in Ureilitic Regolith: Timing

There is currently no reliable method for obtaining precise implantation ages of xenoliths (i.e., the time at which they were acquired) in breccias such as these. The $^{40}Ar/^{39}Ar$ technique is the most useful chronometer for studying impact processes because the high diffusion rate of Ar often results in resetting of the radiometric clock during impacts, when other isotopic systems may not be reset (Swindle et al. 2014). However, resetting is not guaranteed, and $^{40}Ar/^{39}Ar$ may, in fact, record events in the history of xenolithic materials that occurred on their original parent bodies (Turrin et al. 2013, 2015). Furthermore, implantation ages may be reset by later impacts, so that the youngest $^{40}Ar/^{39}Ar$ ages record "breccia closure" times (Fagan et al. 2014) rather than implantation ages. Thus, unambiguous interpretation of $^{40}Ar/^{39}Ar$ ages of xenoliths is difficult.

We can, however, derive strong constraints on the timing of implantation of CC-like xenoliths by considering the history of their host breccias and relationships between the CC xenoliths and other components of these breccias. Based on ^{26}Al–^{26}Mg chronology and thermal modeling, the ureilite parent body (UPB) accreted $\leqslant$1 Myr after CAI and shortly thereafter was rapidly heated by decay of ^{26}Al, experiencing partial melting and rapid melt extraction (Wilson et al. 2008; Baker et al. 2012; Kita et al. 2013; Goodrich et al. 2015a; Van Kooten et al. 2017). Extremely high rates of cooling (accompanied by a large drop in pressure) recorded in all ureilites indicate that this body

was then catastrophically disrupted by a large impact while it was still hot (Warren & Kallemeyn 1992; Mittlefehldt et al. 1998; Goodrich et al. 2004; Downes et al. 2008; Herrin et al. 2010), with subsets of its fragments reassembling into a family of smaller, rubble pile–structured bodies (Michel et al. 2001, 2015). The observation that polymict ureilites show the same range and proportions of ureilite types as the ureilite collection on the whole (Goodrich et al. 2004; Downes et al. 2008) indicates that polymict ureilites developed on these offspring bodies, rather than on the original UPB. The age of ~5.0–5.4 Myr after CAI for the final cooling of ureilitic crustal clasts in polymict ureilites, as well as internal ureilite isochrons, most likely records the time of disruption of the UPB and the time of formation of the offspring bodies (Goodrich et al. 2010, 2015a; Herrin et al. 2010; Amelin et al. 2015). Thus, ~5 Ma after CAI is the earliest possible implantation age for most xenoliths in polymict ureilites.

Johnson et al. (2016) and Scott et al. (2018) noted that the timing and high-energy impact conditions required for the catastrophic disruption of the UPB would be consistent with the Grand Tack, implying that the impactor may have been a C-type body migrating into the inner solar system from beyond the orbit of Jupiter. Further, Scott et al. (2018) and Horstmann & Bischoff (2014) both suggested that the huge diversity of non-ureilitic materials (xenoliths) in AhS could be explained if all of these materials represented local debris (generated because of the high impact frequency environment of the Grand Tack) that reaccreted into the ureilitic offspring bodies along with ureilitic material after the catastrophic disruption. If this is the case, then the implantation ages of almost all xenoliths in polymict ureilites, including the CC-like clasts, would be ~5.0–5.4 Ma after CAI.

However, this scenario is not viable, because many of the observed xenolith types did not exist at 5.0–5.4 Ma after CAI. The xenolithic materials in both AhS and all other polymict ureilites include OC (all groups: H, L, and LL), EC (both groups: EH and EL), and RC of all petrologic types (i.e., metamorphic grades), from type 3 through type 6 (Jaques & Fitzgerald 1982; Prinz et al. 1986, 1987; Ikeda et al. 2000, 2003; Bischoff et al. 2006; Goodrich et al. 2004; Downes et al. 2008; Ross et al. 2010; Horstmann & Bischoff 2014; Goodrich et al. 2015a, 2015b, 2016, 2017a, 2017b, 2019a, 2019b, 2020; Goodrich & Gross 2015; Patzek et al. 2018; Boleaga & Goodrich 2019). Although OC parent bodies accreted at ~2–4 Myr after CAI (Bennett & McSween 1996; Blackburn et al. 2017; Pape et al. 2019; Pedersen et al. 2019), they were heated and metamorphosed slowly, and therefore the higher metamorphic types of OC did not exist until tens of millions of years later. Based on the duration of thermal metamorphism as recorded by Pb-Pb closure ages (Blackburn et al. 2017), type 6 H and L OC did not exist until 50–60 Myr after CAI. Type 5 OC did not exist until ~20 (H) or 30 (L) Myr after CAI, and type 4 did not exist until ~5–7 Myr after CAI (data for H only). It is likely that similar timescales apply to metamorphosed EC and RC, which have textures and equilibration temperatures similar to those of the equivalent petrologic type OC (Dodd 1981; Zhang et al. 1996; Huss et al. 2006; Bischoff et al. 2011; Lingemann et al. 2000). Therefore, only the lowest petrologic type OC, RC, and EC xenoliths in polymict ureilites could have been available to accrete to ureilitic daughter bodies at 5.4 Ma after CAI.

Furthermore, we suggest that it is most likely that OC, RC, and EC xenoliths of all petrologic types, as well as CC-like xenoliths such as those studied here, were all added to the ureilitic daughter bodies at approximately the same time, i.e., within a short time period corresponding to the time that OC parent bodies (both H and L and probably also LL) were catastrophically disrupted and OC materials of all petrologic types were liberated simultaneously, which occurred at ~50–60 Myr after CAI (Blackburn et al. 2017). We hypothesize that EC and RC parent bodies were also catastrophically disrupted at approximately this time, based on their similar thermal histories and following Blackburn et al. (2017), who pointed out that the disruption of both H and L bodies at this time suggests that these impacts were part of a general phenomenon, i.e., a period of enhanced impact frequencies applicable to the asteroid belt as a whole, rather than isolated events. The timing of this period is consistent with the timing of the early instability, inferred to have occurred within ~100 Myr of the dispersion of the gaseous disk, which dynamically stirred the asteroid belt and resulted in an epoch of increased impact velocities (Clement et al. 2018, 2019; de Sousa et al. 2020). The exact timing of the instability is not known. However, de Sousa et al. (2020) obtained median instability times of 37–62 Myr after disk dispersion (~40–67 Myr after CAI) for a range of modeled scenarios, similar to the timing inferred here for the breakup of multiple chondritic bodies in the asteroid belt.

These inferences suggest that all (or at least many) of the varieties of xenoliths in polymict ureilites were acquired during this time period. It cannot be ruled out that some xenoliths, e.g., lower petrologic type OC (or EC or RC), were acquired over the period 5–60 Myr after CAI, having been liberated from their parent bodies by impacts. However, the volume of fragmental materials that were liberated and put into dynamically "excited" states by catastrophic disruption of multiple bodies around 50–60 Myr after CAI would have been much greater than that liberated earlier by sub-catastrophic impacts, and would have greatly enhanced the impactor flux. Additionally, the small scale on which disparate types of xenoliths are mixed in polymict ureilites (OC, CC, and EC clasts of many types and subtypes, as well as several types of achondrites, found within a few millimeters of one another in the same section; e.g., Jaques & Fitzgerald 1982; Ikeda et al. 2000; Goodrich et al. 2004, 2016, 2017b) strongly suggests that they were all intermixed with ureilitic material during the same relatively short time period.

The most remarkable example of this intimate scale of mixing is seen in AhS 91A and AhS 671, and unequivocally supports the acquisition of CC-like xenoliths at the same time as all other types. As discussed in detail in Goodrich et al. (2019a), the C1 material of AhS 91A and AhS 671 is in direct contact with, often completely enclosing, fragments of OC, EC, and ureilitic materials intimately associated with one another (e.g., Figures 7(a)–(d)). The OC fragments include petrologic types 3–5 (based on mineral compositions and textures), and one EC fragment is an EH of petrologic type 6, based on the Ni (3.0 wt.%) and Si (8.2 wt.%) contents of its kamacite (Weyrauch et al. 2018). This association provides irrefutable evidence for dynamically excited mixing between CC reservoir (CC xenolith) and NC reservoir materials (ureilitic, OC, EC fragments) that could not have occurred until tens of millions of years after CAI and therefore did not happen during the Grand Tack (or any gaseous disk model) events. These textural arguments can be extended to CC-like xenoliths in NWA 10657 and other polymict ureilites, although in these other

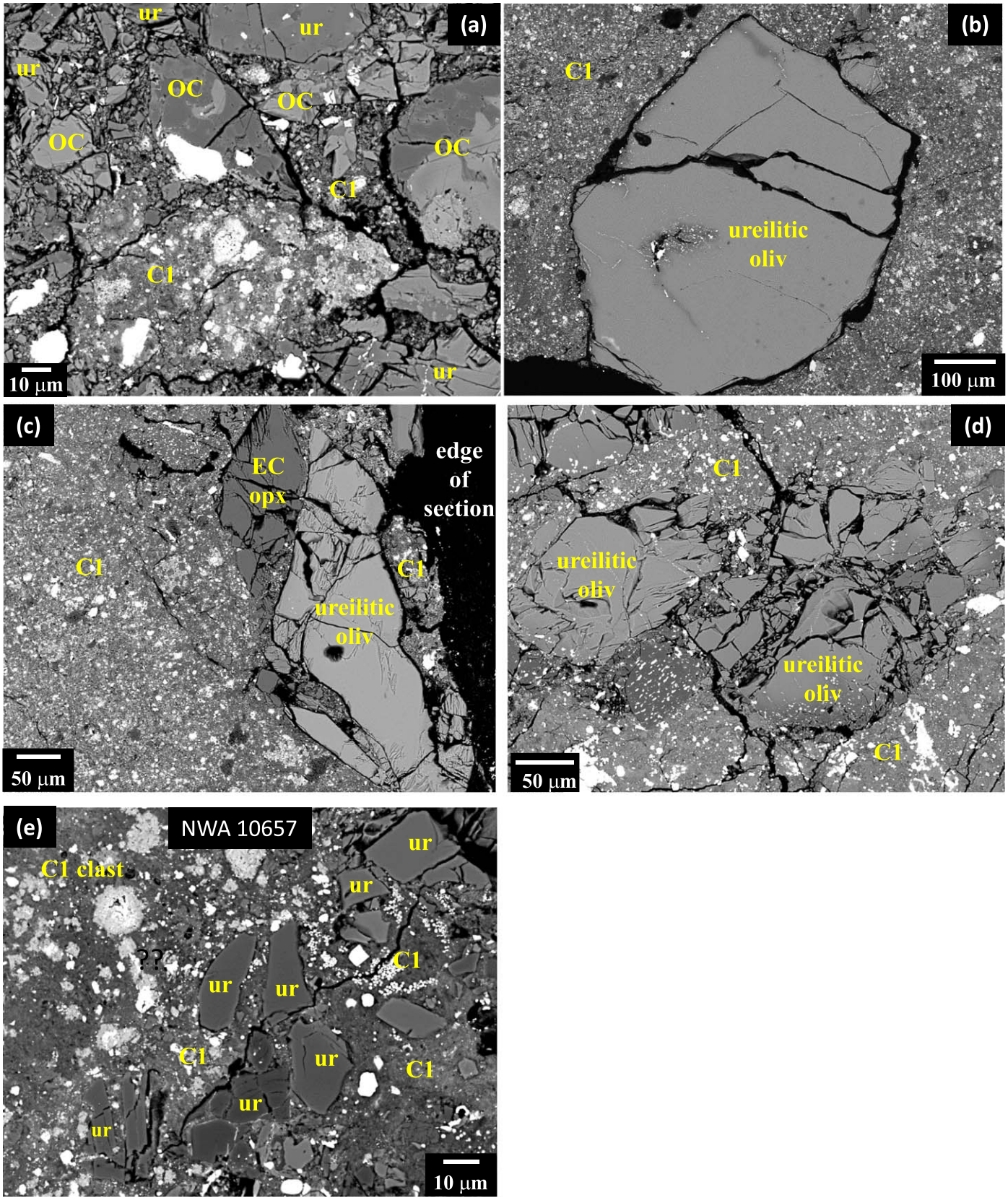

Figure 7. BEIs showing textures of CC-like (C1) lithologies in polymict ureilites in contact with ureilitic (ur), OC, and EC components of their host breccias in polymict ureilites. (a)–(d) AhS 91A or AhS 671. (e) NWA 10657 clast 2, brecciated boundary with surrounding ureilitic materials. opx = orthopyroxene; oliv = olivine.

samples the evidence for intimate scale mixing is less direct. In the sections of NWA 10657 that we have studied, we have so far identified xenoliths of L4-5 and R4-5 chondrites, EC metal, and NWA 7325–like (NC) achondrites (an ungrouped NC achondrite) located within a few millimeters of CC-like xenoliths in the ureilitic host.

These arguments lead us to conclude that CC reservoir xenoliths (at least those studied here) were mixed with a large variety of NC materials in ureilitic regolith within a short time period around ~50–60 Myr after CAI, or shortly thereafter. In the next section, we examine the impact conditions under which they were implanted.

4.3. Implantation of CC-like Xenoliths in Ureilitic Regolith: Impact Conditions

The xenoliths studied here in NWA 10657 show no evidence of chemical or thermal reaction with their immediate surroundings in the host breccia. No reaction rims are observed in backscattered electron images (BEIs), there are no systematic changes in the mineralogy of the xenoliths near contacts with host materials, and compositional profiles normal to contacts show no evidence of increasing dehydration of phyllosilicates (i.e., increasing EMPA totals) approaching the contact. Texturally, contacts between the xenoliths and host material vary from smooth boundaries with adjacent ureilitic silicate grains to brecciated regions containing angular fragments of various ureilitic minerals intimately mixed with CC clast matrix materials (e.g., Figure 7(e)). Furthermore, no evidence of melting of either xenoliths or adjacent host materials has been observed along the contacts.

The stones AhS 91A and AhS 671 constitute a particularly informative example of the intimate scale on which CC reservoir material is intermixed with NC ureilitic, OC, and EC materials in polymict ureilites. These stones show clasts of ureilitic mineral fragments (olivines, pyroxenes, metal, graphite), OC chondrules and chondrule fragments, and EC metal grains completely enclosed within C1 matrix material (Goodrich et al. 2019a). The contacts between the C1 material and the larger ureilitic mineral fragments are smooth, with no evidence of chemical or thermal reactions between the ureilitic and C1 material (e.g., Figures 7(b) and (c); see also Figures 12 and 13 of Goodrich et al. 2019a). Other areas (e.g., Figures 7(a) and (d)) are brecciated and consist of intermixed OC chondrule fragments, angular and fractured ureilitic mineral fragments, and C1 matrix material, similar to the brecciated boundaries of some of the NWA 10657 CC clasts (Figure 7(e)). Of particular importance is that AhS 91A and AhS 671 show direct contacts between CC, OC, EC, and ureilitic materials, whereas at least so far, the CC clasts we have studied in typical polymict ureilites have shown contacts only with ureilitic materials.

These textures strongly suggest that the xenoliths were implanted into their hosts under relatively "gentle" impact (i.e., "low"-velocity) conditions. Rubin & Bottke (2009) reached a similar conclusion regarding "lightly processed" CM-like clasts in H-chondrite and HED breccias. The precise impact velocity needed to avoid dehydrating CC-like impactors depends on the material properties of the impactor and target (e.g., equation of state, porosity) and impact angle. Impact velocities $<\sim 300\ \mathrm{m\ s^{-1}}$ almost certainly implant "lightly processed" xenoliths (e.g., Figure 1 of Bischoff et al. 2006). Tyburczy et al. (1986) measured the shock devolatilization of Murchison (a CM chondrite) and found that devolatilization started at initial shock pressures of ~17 GPa and was complete by ~30 GPa. These pressures can be related to impact velocities using the planar impact approximation and an equation of state (e.g., Gault & Heitowit 1963). Simple estimates indicate that, for a vertical impact, devolatilization of phyllosilicates in CM-type material starts at $\sim 2.5\ \mathrm{km\ s^{-1}}$ and is complete at $\sim 5\ \mathrm{km\ s^{-1}}$.

Pressure and temperature will vary throughout the impactor, with the highest temperatures and pressures near the impact point. Oblique impacts, in particular, lead to a broad range of temperatures and pressures in the projectile (Pierazzo & Melosh 2000; Potter & Collins 2013; Schultz & Eberhardy 2015). For example, Daly & Schultz (2018) recovered clasts of a serpentine impactor that showed no volatile loss or pervasive fracturing after a $5\ \mathrm{km\ s^{-1}}$ impact at 45°, even though other parts of the impactor devolatilized. Such clasts are consistent with the criteria for a lightly processed hydrated xenolith, despite the impact velocity. Nevertheless, at $20\ \mathrm{km\ s^{-1}}$, even a highly oblique impact is exceedingly unlikely to deliver hydrated impactor clasts intact. Svetsov & Shuvalov (2015), for instance, estimated based on 3D impact models that even at $10\ \mathrm{km\ s^{-1}}$, only small regions of stony asteroids could remain hydrated in an oblique impact. In addition, in a highly oblique impact, most of the impactor travels downrange at a significant fraction of the impact velocity (Schultz & Gault 1990), which leads to very little of the impactor being implanted onto the target (Daly & Schultz 2016). Therefore, although in principle it is possible that a highly oblique, very high velocity (i.e., $>5\ \mathrm{km\ s^{-1}}$) impact could create a few clasts that look lightly processed, these clasts are unlikely to have been preserved in the regolith.

Thus, the absence of evidence for dehydration of the CC-like xenoliths during implantation into their hosts suggests impact conditions of $<5\ \mathrm{km\ s^{-1}}$. Such conditions are unlikely to be consistent with the high velocities (up to 20–40 $\mathrm{km\ s^{-1}}$ for some objects) inferred for outer solar system bodies migrating into the inner solar system during the very dynamically exciting Grand Tack event (Johnson et al. 2016), or during post–gas giant planet instabilities (Tsiganis et al. 2005; Clement et al. 2018, 2019). It is plausible that a C-type body in the process of being emplaced in the inner solar system was responsible for catastrophic disruption of the UPB at ~5 Myr after CAI, as suggested by Johnson et al. (2016) and Scott et al. (2018). However, the CC-like xenoliths that we are studying cannot be remnants of that impactor, which is likely to have been mostly melted and/or volatilized due to the high impact velocities. We conclude that the CC-like xenoliths studied here were not implanted into their host asteroids directly by bodies in the process of migrating inward from the outer solar system. Instead, they must have been implanted under similar conditions as the NC xenoliths, and therefore likely derived from CC-like bodies that were already present in orbits in the inner solar system.

As discussed above, the inferred timing of implantation of most xenoliths is consistent with the timing of the Early Instability model. Excitation of the asteroid belt during this period (Clement et al. 2018, 2019) could have been responsible for catastrophic disruption of a number of chondritic parent bodies around 40–60 Myr after CAI. Disruption of each of these bodies would have resulted in reaccumulation of the debris to form a family of rubble-pile bodies (Michel et al. 2001, 2004, 2015). Thus, multiple chondritic types of families (e.g., H, L, LL, EH, EL, and RC) could have been created at this time. Furthermore, each rubble pile likely contained a mix of petrographic grades of its chondrite type (e.g., mixed LL materials of types 3–6). Intrafamily mixing could also have been enhanced by a high probability of low-velocity intrafamily collisions soon after family formation (Bottke et al. 1994). After the family members were dispersed, however, they would have become main belt asteroids in their own right, and so

(assuming the peak of the instability has died down) would show the typical main belt distribution of impact velocities with a mean of ~5 km s^{-1} (e.g., Bottke et al. 1994).

Sub-catastrophic impacts of a variety of these chondritic rubble-pile bodies with the ureilitic rubble-pile bodies, all within a short time period, could have resulted in implantation of xenoliths (surviving fragments of the impactors) to form highly contaminated, mixed regolith layers (that became the polymict ureilites) on the ureilitic bodies. Alternatively, impactor materials could have been added during disruption and reassembly of the ureilitic rubble-pile bodies themselves, i.e., second- (or higher-order) generation catastrophic disruption/reassembly events (e.g., Bottke et al. 2020; Walsh et al. 2020). This would require multiple disruption/reassembly events, each due to a different impactor type, to explain the large variety of xenolithic materials. Remixing of all materials during each reassembly event could potentially lead to the observed intimate scale on which diverse chondritic and ureilitic clasts are mixed. In either case, further experimental work is needed to determine what range of impact conditions is required to produce all of the observed characteristics of the various types of xenoliths and whether such conditions are consistent with the typical main belt distribution of impact velocities. In addition, more detailed petrographic studies of polymict ureilites should be conducted to determine whether some xenoliths show small amounts of melt or other shock features that have not been recognized so far.

These uncertainties do not, however, impact our principal conclusion, which is that the absence of dehydration, or other evidence of heating or shock, in the CC xenoliths studied so far makes it unlikely that they were implanted into their host asteroids by bodies in the process of migrating inward from the outer solar system. Instead, they must have been implanted under similar conditions as the NC xenoliths, and therefore derived from CC-like bodies that were already present in orbits in the inner solar system.

4.4. Derivation from C-type or D–T–P-type Asteroids?

If the asteroidal bodies from which the CC-like xenoliths in polymict ureilites were derived originated in the outer solar system, they could have been emplaced in inner solar system orbits during the gaseous disk phase (Raymond & Izidoro 2017), or in the early stages (i.e., between ~5 and 50 Myr after CAI) of an early instability period (Clement et al. 2018, 2019). In this section, we consider which of these is more likely.

Dynamical models that describe the gaseous disk phase (such as Grand Tack or rapid giant planet formation) and those that describe a later period of "global" instability (Nice Model or Early Instability) both result in transfer of outer solar system materials into the inner solar system. However, the former transfer C-type bodies from between and beyond the orbits of Jupiter and Saturn (e.g., Walsh et al. 2012), while the latter transfer trans-Neptunian bodies inferred to be D, P, or T types (Levison et al. 2009). Thus, under the assumption that the CC-like xenoliths in polymict ureilites (or any NC breccia) originated in the outer solar system, one criterion for distinguishing which of these types of dynamical instability they are associated with (i.e., during which of these time periods they were transferred) is whether they more closely resemble C type(s) or D, P, and T types of asteroids. The C-complex asteroids are commonly associated with various types of carbonaceous chondrites based on comparison of their visible to near-infrared (VNIR) reflectance spectra with those measured for the meteorites in the laboratory (DeMeo et al. 2009, 2015). The D-, T-, and P-type asteroids are thought to be either very rich in organics and opaques (Gradie & Veverka 1980), or very strongly space weathered (Emery & Brown 2003, 2004), and do not seem to be widely represented in our meteorite collections. The only meteorite whose reflectance spectrum has ever been found to resemble D-, T-, or P-type asteroids is the ungrouped C2 chondrite Tagish Lake (Hiroi et al. 2001).

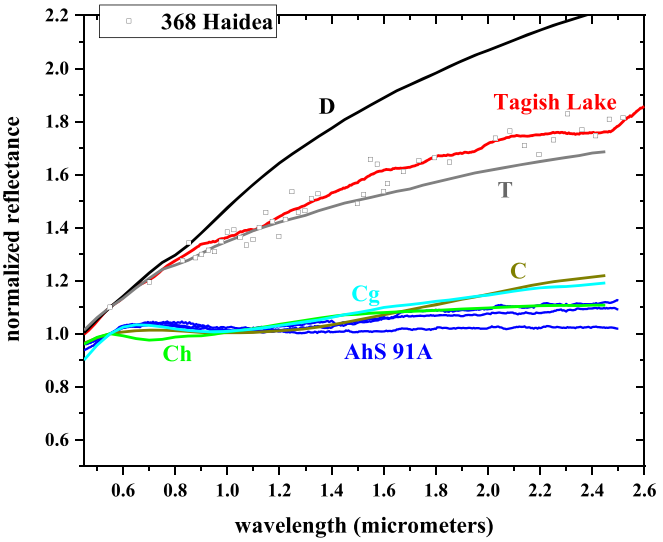

Figure 8. VNIR reflectance spectra of chips and powders of AhS 91A (Goodrich et al. 2019a) and the ungrouped C2 chondrite Tagish Lake (Hiroi et al. 2001) compared with class means for C, Ch, Cg, D, and T asteroids from DeMeo et al. (2009). Reflectance values for all spectra are normalized to 1 at 0.55 μm. Spectra for Tagish Lake and D and T means are additionally slightly offset. Also shown for comparison is the spectrum of asteroid 368 Haidea, which was classified as a D-type asteroid in Tholen taxonomy and noted by Hiroi et al. (2001) as a good match to Tagish Lake.

The VNIR reflectance spectrum of AhS 91A (Goodrich et al. 2019a) is dark, relatively flat, and featureless (lacking strong absorptions), very similar to several C-complex asteroid types and therefore quite unlike the very red-sloped spectra of D, P, or T asteroid types (Figure 8). The AhS 91A–type lithology is also quite distinct from Tagish Lake in mineralogy (Brown et al. 2000; Zolensky et al. 2002; Hildebrand et al. 2006), oxygen and chromium isotope compositions (Figure 1), and D/H ratios (Figure 6). Thus, if the CC-like xenoliths in polymict ureilites originated in the outer solar system, they were probably derived from C-type asteroids transferred from between and beyond the orbits of Jupiter and Saturn to the inner solar system during the gaseous disk phase. The D/H ratios are consistent with this conclusion. The high δD values of the phyllosilicates (Figure 6) in the AhS 91A/671–type lithology (with even higher values inferred if organics were included), along with the data of Patzek et al. (2020) for CC-like clasts in polymict ureilites, would suggest that these bodies originated further out in the solar system than known CCs (Alexander 2017). However, the observed values (even those of Patzek et al. 2020 including organics) are not extreme, which supports the conclusion of Alexander (2017) that CCs, including the xenoliths studied here, did not form further out than the orbit of Saturn in the disk.

4.5. Summary

Results of chromium, oxygen, and hydrogen isotope analyses, combined with petrologic observations, for several carbonaceous chondrite-like xenoliths in polymict ureilites show that they are derived from the CC isotopic reservoir and became intimately mixed with a variety of NC reservoir materials (including OC, EC, RC, ureilitic, and other achondritic types) in ureilitic asteroidal regolith. Furthermore, these xenoliths appear to represent several unique lithologies that have not been sampled as whole meteorites on Earth.

Based on the textural and petrologic characteristics of these xenoliths and their relationships to other components of their host breccias, we argue that most xenoliths of CC, OC, EC, RC, and other materials were all implanted into ureilitic regolith as remnants of impactors ~50–60 Myr after CAI or shortly thereafter. The impactors were produced by catastrophic disruption/reassembly of multiple chondritic parent bodies in the asteroid belt at this time. This timing is consistent with the timing of the Early Instability model for a period of enhanced impact velocities in the asteroid belt (Clement et al. 2018, 2019; de Sousa et al. 2020), as opposed to the Nice Model (Gomes et al. 2005; Tsiganis et al. 2005).

The CC-like xenoliths (like the others) were implanted into the regolith under relatively "gentle" impact conditions, i.e., $<5\,\mathrm{km\,s^{-1}}$, consistent with being fragmentary debris from these local disruptions, rather than directly from outer solar system bodies plunging into the inner solar system during an instability and resulting in huge impact velocities. This implies that the CC bodies were already present in the asteroid belt. VNIR reflectance spectra show that these xenoliths resemble C-complex asteroids, rather than D, T, or P types. Therefore, if the NC versus CC isotopic dichotomy corresponds to inner versus outer solar system formation locations (Kruijer et al. 2017; Bryson et al. 2020), the parent asteroids of these xenoliths were probably emplaced in the inner solar system during the gaseous disk phase (Raymond & Izidoro 2017). On the other hand, our observations are also consistent with these bodies having formed in the inner solar system in the first place, permitting other interpretations of the NC versus CC dichotomy (Huss 2019). Discussion of such models is beyond the scope of this paper.

We thank Takahiro Hiroi and David Kring for helpful discussions and Anna Maria Fioretti for initial observations of AhS 91A and AhS 671. We are grateful to Dave Draper and Lindsay Keller for making the ARES JSC electron beam facilities available for this work and D. Kent Ross for assistance with electron microprobe analyses. This work was supported by NASA EW grants NNX17AH09GS03 and 80NSSC19K0507 to C.A.G. and NNX16AD34G to Q.Z.Y. and a NASA EW grant to M.Z. This is Lunar and Planetary Institute publication #2581.

Appendix
Analytical Techniques

A.1. Chromium Isotope Analyses

Chromium isotopic analyses were completed on three different sample aliquots: small internal fragments of AhS 91A and AhS 671 and an aliquot extracted from clast 28 found within NWA 10657. The fragments of AhS 91A and AhS 671 were visually inspected to ensure no visible fusion crust or terrestrial weathering product was present on the fragment to be processed and then were crushed and homogenized using an agate mortar and pestle.

Figure A1. Clast 28 of NWA 10657 on the surface of the slab. Optical photomicrograph.

For clast 28 of NWA 10657, optical microscopy was used to visualize the clast (Figure A1) and identify material for extraction. Small pieces of the internal portion of the clast were extracted using a metal dental tool, ensuring that no matrix material was adhered, by minimizing material from the outer edge of the clast. A small fragment was taken for Cr isotopic measurements, while material from the same clast was reserved for oxygen and petrographic analyses. Following extraction, the fragment from clast 28 was also crushed and homogenized using an agate mortar and pestle. The resulting sample powders of AhS 91A (24.77 mg), AhS 671 (10.84 mg), and clast 28 of NWA 10657 (3.16 mg) were transferred to individual PTFE Parr capsules along with a 3:1 mixture of concentrated HF and HNO_3. The PTFE capsules were sealed in stainless steel jackets and heated in a 190°C oven for 96 hr to ensure complete dissolution of silicate and refractory phases. After complete dissolution, the samples were processed through a three-column ion chromatography separation procedure as described in Yamakawa et al. (2009). The isotopic compositions of the purified Cr fractions were analyzed using a Thermo *Triton Plus* thermal ionization mass spectrometer at the University of California, Davis. Details of the mass spectrometry procedure are given in Sanborn et al. (2019). All Cr isotopic data are reported as parts per 10,000 deviation (ε-notation) from the terrestrial composition as represented by NIST SRM 979, analyzed in the same analytical session.

A.2. Oxygen Isotope Analyses

Oxygen isotope data for AhS 91A and AhS 671 were reported in Goodrich et al. (2019a). The analytical techniques used here for NWA 10657 clast 28 were the same as described in that paper.

A.3. Hydrogen Isotope Analyses

Hydrogen isotope analysis was performed with the Cameca 1280 ion microprobe equipped with a Hyperion II RF plasma ion source at the University of Hawai'i, Manoa. A $^{16}O^-$ primary beam accelerated to −13 keV was set to ~4 nA and defocused to ~30 μm. Positive secondary ions of hydrogen isotopes, $^{12}C^+$, $^{24}Mg^{2+}$, and $^{30}Si^+$ were measured in monocollection mode with

an electron multiplier. A field aperture gating was selected to collect secondary ions only from an $\sim 4 \times 4\ \mu$m area in the center of the beam, excluding H ions from beam crater edges. A mass resolving power of ~2000 effectively resolved signals from D^+ and H_2^+. Measurements consisted of 20 cycles, and H^+, D^+, $^{12}C^+$, $^{24}Mg^{2+}$, and $^{30}Si^+$ were measured each cycle for 3, 40, 1, 1, and 1 s, respectively. During 500 s of presputtering, we imaged H^+ with the field aperture opened, allowing us to observe the H distribution over the entire 30 μm region being sputtered. Small adjustments to the beam position were made in order to avoid anhydrous grains in the matrix and center the beam on H-rich areas. These fine-grained phyllosilicate "packets" were measured in the matrices of all samples. Coarse-grained phyllosilicates devoid of anhydrous phases were measured in AhS 671-03 and AhS 91A. Time interpolation was performed to correct for monocollection, and dead-time corrections were applied assuming an electron multiplier dead time of 30 ns. A terrestrial chrysotile standard characterized by Alt & Shanks (2006) was selected to determine the instrumental mass fractionation (IMF) of H isotopes. The standard was measured three times before and after the sample measurements each day in order to monitor the IMF drift. All samples except NWA 10657 clast 2 were measured in the same session, and the IMF was not observed to drift during this session. We therefore averaged 43 standard measurements to determine the IMF for the first session. Clast 2 of NWA 10657 was measured in a different session, and the IMF was determined from the average of six standard measurements. Reported errors for each measurement are the greater of the standard error calculated from the individual cycles and the statistical counting error after summing the counts from all cycles.

In the matrices of CCs, fine-grained phyllosilicates are intergrown with D-rich organic materials at a submicron scale (Le Guillou & Brearley 2013; Le Guillou et al. 2014), and phyllosilicates cannot be exclusively targeted with the current method. However, primary $^{16}O^-$ ions ionize H in phyllosilicates ~330–500× more efficiently than H in organics (Deloule & Robert 1995; Bonal et al. 2010). We also note that in C1 and C2 lithologies, phyllosilicates are much more abundant than organics, so our D/H measurements primarily reflect the composition of structurally bound hydroxyl and interlayer H_2O in phyllosilicates.

Several procedures were carried out to minimize contamination from terrestrial H. The sample chamber was baked prior to measurements and pumped down to $\leqslant 10^{-10}$ torr with an LN_2 cold trap in the sample chamber. Samples were stored in a vacuum oven at ~58°C for at least 3 days to allow adsorbed water to dissipate and then immediately transferred to the ion probe's airlock chamber, where they remained overnight to facilitate outgassing of the epoxy embedding medium. After the initial standard measurements, the samples were loaded into the sample chamber, and measurements did not commence until the vacuum again reached $\leqslant 10^{-10}$ torr. Our presputtering time (500 s) removed the vast majority of the C coating, except for residual C that infiltrated small cracks and pore spaces. Residual C remaining after the presputter was easily identified in plots of $^{12}C/H$ versus cycle number, when the $^{12}C/H$ ratio was observed to decrease exponentially over the first few cycles before reaching a constant value. In this case, the first cycles with decreasing $^{12}C/H$ were eliminated from calculations of D/H, ensuring that terrestrial H bound to the C coating was not included in our calculations.

A.4. SEM and EMPA

Petrologic data for AhS 91A and AhS 671 were reported in Goodrich et al. (2019a). The analytical methods used here for NWA 10657 were the same as described in that paper.

ORCID iDs

Cyrena A. Goodrich https://orcid.org/0000-0002-9820-3329
Qing-Zhu Yin https://orcid.org/0000-0002-4445-5096
Kevin J. Walsh https://orcid.org/0000-0002-0906-1761
Edward R. D. Young https://orcid.org/0000-0002-1299-0801

References

Alexander, C. M. O'D. 2017, RSPTA, 375, 20150384
Alexander, C. M. O'D., Bowden, R., Fogel, M. L., et al. 2012, Sci, 337, 721
Alexander, C. M. O'D., Fogel, M., Yabuta, H., & Cody, G. D. 2007, GeCoA, 71, 4380
Alexander, C. M. O'D., Greenwood, R. C., Bowden, R., et al. 2018, GeCoA, 221, 406
Alexander, C. M. O'D., Newsome, S. D., Fogel, M. L., et al. 2010, GeCoA, 74, 4417
Alt, J. C., & Shanks, W. C., III 2006, E&PSL, 242, 272
Amelin, Y., Koefoed, P., Bischoff, A., et al. 2015, LPICo, 1856, 5344
Baker, J. A., Schiller, M., & Bizzarro, M. 2012, GeCoA, 77, 415
Bennett, M. E., & McSween, H. Y., Jr. 1996, M&PS, 31, 783
Bischoff, A., Ebert, S., Patzek, M., et al. 2015, LPICo, 1856, 5092
Bischoff, A., Ebert, S., Patzek, M., et al. 2016, LPICo, 1921, 6319
Bischoff, A., Kraemer, A.-K., Klemm, K. I., et al. 2018a, LPICo, 2067, 6108
Bischoff, A., Lentfort, S., Möhlmann, K., et al. 2019, LPICo, 2157, 6030
Bischoff, A., Schleiting, M., Wieler, R., & Patzek, M. 2018b, GeCoA, 238, 516
Bischoff, A., Scott, E. R. D., Metzler, K., & Goodrich, C. A. 2006, in Meteorites and the Early Solar System II, ed. D. S. Lauretta & H. Y. McSween (Tucson, AZ: Univ. Arizona Press), 679
Bischoff, A., Vogel, N., & Roszjar, J. 2011, ChEG, 71, 101
Blackburn, T., Alexander, C. M. O'D., Carlson, R., & Elkins-Tanton, L. T. 2017, GeCoA, 200, 201
Boleaga, Y., & Goodrich, C. A. 2019, LPSC, 50, 1622
Bonal, L., Alexander, C. M. O'D., Huss, G. R., et al. 2013, GeCoA, 106, 111
Bonal, L., Huss, G. R., Krot, A. N., et al. 2010, GeCoA, 74, 6590
Bottke, W., Nolan, M. C., Greenberg, R., et al. 1994, Icar, 107, 255
Bottke, W., Walsh, K., Vokrouhlicky, D., & Nesvorny, D. 2020, AAS/DPS Meeting, 52, 402.02
Bouvier, A., Gattacceca, J., Grossman, J., & Metzler, K. 2017, M&PS, 52, 2411
Brasser, R., & Mojzsis, S. J. 2020, NatAs, 4, 492
Brearley, A. J., & Prinz, M. 1992, GeCoA, 56, 1373
Brown, P. G., Hildebrand, A. R., Zolensky, M. E., et al. 2000, Sci, 290, 320
Bryson, J. F. J., Weiss, B. P., Biersteker, J. B., et al. 2020, ApJ, 896, 103
Budde, G., Burkhardt, C., Brennecka, G. A., et al. 2016, E&PSL, 454, 293
Burkhardt, C., Kleine, T., Oberli, F., et al. 2011, E&PSL, 312, 390
Clayton, R. N., & Mayeda, T. K. 1996, GeCoA, 60, 1999
Clayton, R. N., & Mayeda, T. K. 1999, GeCoA, 63, 2089
Clayton, R. N., Mayeda, T. K., Goswami, J. N., & Olsen, E. J. 1991, GeCoA, 55, 2317
Clayton, R. N., Mayeda, T. K., & Rubin, A. E. 1984, JGR, 89, C245
Clement, M. S., Kaib, N. A., Raymond, S. N., & Walsh, K. J. 2018, Icar, 311, 340
Clement, M. S., Kaib, N. A., Raymond, S. N., & Walsh, K. J. 2019, Icar, 321, 778
Daly, R. T., & Schultz, P. H. 2016, Icar, 264, 9
Daly, R. T., & Schultz, P. H. 2018, M&PS, 53, 1364
Dauphas, N., & Schauble, E. A. 2016, AREPS, 44, 709
Deer, W. A., Howie, R. A., & Zussman, J. 1962, Rock Forming Minerals, Vol. 3. Sheet Silicates (London: Longman Group Limited), 269
Deloule, E., & Robert, F. 1995, GeCoA, 22, 4695
DeMeo, F. E., Alexander, C. M. O'D., Walsh, K. J., et al. 2015, in Asteroids IV, ed. P. Michel, F. E. DeMeo, & W. F. Bottke (Tucson, AZ: Univ. Arizona Press), 13
DeMeo, F. E., Binzel, R. P., Slivan, S. M., & Bus, S. J. 2009, Icar, 202, 160
de Sousa, R. R., Morbidelli, A., Raymond, S. N., et al. 2020, Icar, 339, 113605

Dodd, R. T. 1981, Nat, 290, 189
Downes, H., Mittlefehldt, D. W., Kita, N. T., & Valley, J. W. 2008, GeCoA, 72, 4825
Emery, J. P., & Brown, R. H. 2003, Icar, 164, 104
Emery, J. P., & Brown, R. H. 2004, Icar, 170, 131
Engrand, C., Gounelle, M., Zolensky, M. E., & Duprat, J. 2003, LPSC, 34, 1688
Fagan, A., Joy, K. H., Bogard, D. D., & Kring, D. A. 2014, EM&P, 112, 59
Fleet, M. 2003, Rock Forming Minerals, Vol. 3A. Sheet Silicates: Micas (2nd ed.; London: The Geological Society)
Fodor, R. V., & Keil, K. 1976, GeCoA, 40, 177
Fodor, R. V., Keil, K., Wilkening, L. L., et al. 1976, in Tectonics and Mineral Resources of Southwestern North America, New Mexico Geological Society Special Publication No. 6, ed. L. A. Woodward (Socorro, NM: New Mexico Geological Society), 206
Fredriksson, K., Jarosewich, E., & Nelen, J. 1969, in Meteorite Research, ed. P. M. Millman (Dordrecht: D. Reidel), 155
Funk, S. C., Bischoff, A., & Schlüter, J. 2011, M&PSA, 74, 5318
Gault, D. E., & Heitowit, E. D. 1963, The Partition of Energy for Hypervelocity Impact Craters Formed in Rock (Alexandria, VA: Defense Documentation Center for Scientific and Technical Information)
Gomes, R., Levison, H. F., Tsiganis, K., & Morbidelli, A. 2005, Nat, 435, 466
Goodrich, C. A., Fioretti, A. M., Zolensky, M., et al. 2018, LPSC, 49, 1321
Goodrich, C. A., & Gross, J. 2015, LPSC, 46, 1214
Goodrich, C. A., Hamilton, V. E., Zolensky, M. E., et al. 2020, LPSC, 51, 1223
Goodrich, C. A., Hartmann, W. K., O'Brien, D. P., et al. 2015a, M&PS, 50, 782
Goodrich, C. A., Hutcheon, I. D., Kita, N. T., et al. 2010, E&PSL, 295, 531
Goodrich, C. A., Kita, N. T., Yin, Q.-Z., et al. 2017a, GeCoA, 203, 381
Goodrich, C. A., Mikouchi, T., & Treiman, A. H. 2015b, LPICo, 1856, 5048
Goodrich, C. A., Ross, D. K., & Treiman, A. H. 2017b, LPSC, 48, 1101
Goodrich, C. A., Scott, E. R. D., & Fioretti, A. M. 2004, ChEG, 64, 283
Goodrich, C. A., Treiman, A. H., Kita, N. T., & Defouilloy, C. 2016, LPSC, 47, 1617
Goodrich, C. A., Zolensky, M., Fioretti, A. M., et al. 2019a, M&PS, 54, 2769
Goodrich, C. A., Zolensky, M., Kohl, I., et al. 2019b, LPSC, 50, 1312
Gounelle, M., Engrand, C., Alard, O., et al. 2005, GeCoA, 69, 3431
Gounelle, M., Zolensky, M. E., Liou, J.-C. L., et al. 2003, GeCoA, 67, 507
Gradie, J., & Veverka, J. 1980, Nat, 283, 840
Greshake, A. 2014, M&PS, 49, 824
Hamilton, V. E., Goodrich, C. A., Treiman, A., et al. 2020a, LPSC, 51, 1122
Hamilton, V. E., Goodrich, C. A., Treiman, A. H., et al. 2020b, NatAs
Herrin, J. S., Zolensky, M. E., Ito, M., et al. 2010, M&PS, 45, 1789
Hildebrand, A. R., McCausland, P. J. A., Brown, P. G., et al. 2006, M&PS, 41, 407
Hiroi, T., Zolensky, M. E., & Pieters, C. M. 2001, Sci, 293, 2234
Horstmann, M., & Bischoff, A. 2014, ChEG, 74, 149
Huss, G. R. 2019, LPICo, 2157, 6200
Huss, G. R., Rubin, A. E., & Grossman, J. N. 2006, in Meteorites and the Early Solar System II, ed. D. S. Lauretta & H. Y. McSween (Tucson, AZ: Univ. Arizona Press), 567
Ikeda, Y., Kita, N. T., Morishita, Y., & Weisberg, M. K. 2003, AMR, 16, 105
Ikeda, Y., Prinz, M., & Nehru, C. E. 2000, AMR, 13, 177
Jaques, A. L., & Fitzgerald, M. J. 1982, GeCoA, 46, 893
Jenniskens, P., Fries, M. D., Yin, Q.-Z., et al. 2012, Sci, 338, 1583
Jenniskens, P., Rubin, A. E., Yin, Q.-Z., et al. 2014, M&PS, 49, 1388
Jenniskens, P., Shaddad, M. H., Numan, D., et al. 2009, Nat, 458, 485
Johnson, B. C., Walsh, K. J., Minton, D. A., et al. 2016, SciA, 2, e1601658
Kebukawa, Y., Zolensky, M. E., Ito, M., et al. 2019, LPSC, 50, 1359
Keil, K., & Fodor, R. V. 1980, ChEG, 39, 1
Kerridge, J. F. 1985, GeCoA, 49, 1707
King, A., Bates, H., Krietsch, D., et al. 2019, GhEG, 79, 125531
Kita, N. T., Yin, Q.-Z., MacPherson, G. J., et al. 2013, M&PS, 48, 1383
Kretke, K. A., Bottke, W. F., Levison, H. F., & Kring, D. A. 2017, LPICo, 2043, 2027
Kruijer, T. S., Burkhardt, C., Budde, G., & Kleine, T. 2017, PNAS, 114, 6712
Le Guillou, C., Bernard, S., Brearley, A. J., & Remusat, L. 2014, GeCoA, 131, 368
Le Guillou, C., & Brearley, A. J. 2013, GeCoA, 131, 344
Levison, H. F., Bottke, W. F., Gounelle, M., et al. 2009, Nat, 460, 364
Li, S., Yin, Q.-Z., Bao, H., et al. 2018, GeCoA, 242, 82
Lingemann, C. M., Berlin, J., & Stöffler, D. 2000, M&PSA, 35, A98
Michel, P., Benz, W., & Richardson, D. C. 2004, Icar, 168, 420
Michel, P., Benz, W., Tanga, P., & Richardson, D. C. 2001, Sci, 294, 1696
Michel, P., Jutzi, M., Richardson, D. C., et al. 2015, P&SS, 107, 24
Mittlefehldt, D. W., McCoy, T. J., Goodrich, C. A., & Kracher, A. 1998, in Planetary Materials, ed. J. J. Papike (Chantilly, VA: Mineralogical Society of America), 195
Morbidelli, A., Levison, H. F., Tsiganis, K., & Gomes, R. 2005, Natur, 435, 462
Nanne, J. A. M., Nimmo, F., Cuzzi, J. N., & Kleine, T. 2019, E&PSL, 511, 44
Nozette, S., & Wilkening, L. L. 1982, GeCoA, 46, 557
Pape, J., Mezger, K., Bouvier, A.-S., & Baumgartner, L. P. 2019, GeCoA, 244, 416
Patzek, M., Bischoff, A., Visser, R., & John, T. 2018, M&PS, 53, 2519
Patzek, M., Hoppe, P., Bischoff, A., et al. 2017, LPICo, 1987, 6183
Patzek, M., Hoppe, P., Bischoff, A., et al. 2020, GeCoA, 272, 177
Patzek, M., Kadlag, Y., Bischoff, A., et al. 2019, LPICo, 2157, 6027
Pedersen, S. G., Schiller, M., Connelly, J. N., & Bizzarro, M. 2019, M&PS, 54, 1215
Piani, L., Robert, F., & Remusat, L. 2015, E&PSL, 415, 151
Pierazzo, E., & Melosh, H. J. 2000, M&PS, 35, 117
Poole, G. M., Rehkämper, M., Coles, B., et al. 2017, E&PSL, 473, 215
Popova, O. P., Jenniskens, P., Emel'yanenko, V., et al. 2013, Sci, 342, 1069
Potter, R. W. K., & Collins, G. S. 2013, M&PS, 48, 744
Prinz, M., Weisberg, M. K., Nehru, C. E., & Delaney, J. S. 1986, LPSC, 17, 681
Prinz, M., Weisberg, M. K., Nehru, C. E., & Delaney, J. S. 1987, Metic, 22, 482
Qin, L., Rumble, D., Alexander, C. M. O'D., et al. 2010, M&PS, 45, 1771
Raymond, S. N., & Izidoro, A. 2017, Icar, 297, 134
Robert, F., & Epstein, S. 1982, GeCoA, 46, 81
Ross, A. J., Downes, H., Smith, C. L., & Jones, A. P. 2010, LPSC, 41, 2361
Rubin, A. E., & Bottke, W. F. 2009, M&PS, 44, 701
Rubin, A. E., Kallemeyn, G. W., & Wasson, J. T. 2002, GeCoA, 66, 3657
Sanborn, M. E., Wimpenny, J., Wiliams, C. D., et al. 2019, GeCoA, 245, 577
Sanborn, M. E., Yin, Q.-Z., Goodrich, C. A., et al. 2017, LPICo, 1987, 6277
Schultz, P. H., & Eberhardy, C. A. 2015, Icar, 248, 448
Schultz, P. H., & Gault, D. E. 1990, in Global Catastrophes in Earth History; An Interdisciplinary Conference on Impacts, Volcanism, and Mass Mortality, ed. V. L. Sharpton & P. D. Ward (Boulder, CO: Geological Society of America), 239
Scott, E. R. D., Krot, A. N., & Sanders, I. S. 2018, ApJ, 854, 164
Shaddad, M. H., Jenniskens, P., Numan, D., et al. 2010, M&PS, 45, 1618
Shukolyukov, A., & Lugmair, G. W. 2006, LPSC, 37, 1478
Svetsov, V. V., & Shuvalov, V. V. 2015, P&SS, 117, 444
Swindle, T. D., Kring, D. A., & Weirich, J. R. 2014, GSLSP, 378, 333
Tonui, E., Zolensky, M., Hiroi, T., et al. 2014, GeCoA, 126, 284
Trinquier, A., Birck, J.-L., & Allègre, C. J. 2007, ApJ, 655, 1179
Trinquier, A., Elliott, T., Ulfback, D., et al. 2009, Sci, 324, 373
Tsiganis, K., Gomes, R., Morbidelli, A., & Levison, H. 2005, Nat, 435, 459
Turrin, B. D., Herzog, G. F., & Park, J. 2013, M&PSA, 76, 5335
Turrin, B. D., Lindsay, F. N., Herzog, G. F., et al. 2015, LPSC, 46, 2784
Tyburczy, J. A., Frisch, B., & Ahrens, T. J. 1986, E&PSL, 80, 201
Ueda, T., Yamashita, K., & Kita, N. 2006, M&PSA, 69, 5178
Van Kooten, E. M. M. E., Schiller, M., & Bizzarro, M. 2017, GeCoA, 208, 1
Vokrouhlický, D., Bottke, W. F., & Nesvorný, D. 2016, AJ, 152, 39
Walsh, K. J., Ballouz, R.-L., Bottke, W. F., et al. 2020, LPSC, 51, 2253
Walsh, K. J., Morbidelli, A., Raymond, S. N., et al. 2011, Nat, 475, 206
Walsh, K. J., Morbidelli, A., Raymond, S. N., et al. 2012, M&PS, 47, 1941
Warren, P. H. 2011, GeCoA, 75, 6912
Warren, P. H., & Kallemeyn, G. W. 1992, Icar, 100, 110
Weyrauch, M., Horstmann, M., & Bischoff, A. 2018, M&PS, 53, 394
Williams, C. D., Sanborn, M. E., Defouilloy, C., et al. 2020, PNAS, 117, 23426
Wilson, L., Goodrich, C. A., & Van Orman, J. A. 2008, GeCoA, 72, 6154
Worsham, E., Burkhardt, C., Budde, G., et al. 2019, E&PSL, 521, 103
Yamakawa, A., Yamashita, K., Makashima, A., & Nakamura, E. 2010, ApJ, 720, 150
Yamakawa, A., Yamashita, K., Makishima, A., & Nakamura, E. 2009, AnaCh, 81, 9787
Yin, Q.-Z., Sanborn, M. E., Goodrich, C. A., et al. 2018, LPSC, 49, 1810
Yin, Q.-Z., Yamashita, K., Yamakawa, A., et al. 2009, LPSC, 40, 2006
Zhang, Y., Huang, S., Schneider, D., et al. 1996, M&PS, 31, 87
Zolensky, M. E., Gounelle, M., Briani, G., et al. 2008, M&PSA, 43, 5265
Zolensky, M. E., Nakamura, K., Gounelle, M., et al. 2002, M&PS, 37, 737
Zolensky, M. E., Weisberg, M. K., Buchanan, P. C., & Mittlefehldt, D. W. 1996, M&PS, 31, 518
Zolotov, M. Y., Mironenko, M. V., & Shock, E. L. 2006, M&PS, 41, 1775